Power Electronic Systems
Laboratory

IEEE Transactions on Industrial Electronics, Vol. 64, No. 4, pp. 2982-2991, April 2017

Active Magnetic Damper for Ultrahigh-Speed Permanent-Magnet Machines With Gas Bearings

A. Looser,
A. Tüysüz,
C. Zwyssig,
J. W. Kolar

Eidgenössische Technische Hochschule Zürich
Swiss Federal Institute of Technology Zurich

Active Magnetic Damper for Ultrahigh-Speed Permanent-Magnet Machines With Gas Bearings

Andreas Looser, *Member, IEEE*, Arda Tüysüz, *Member, IEEE*, Christof Zwyssig, *Member, IEEE*, and Johann W. Kolar, *Fellow, IEEE*

***Abstract*—Ultrahigh-speed electrical drive systems enable small-scale electrically driven turbo-compressors for industrial applications, such as fuel cells and heat pumps, due to their compact size, high power density, and high efficiency, in combination with oil-free operation. However, a major obstacle in the industrial implementation of such turbo-machinery is the lack of bearing technologies suited for high rotational speeds. Promising bearing candidates for long lifetime at high rotational speeds are contactless bearing types, such as gas bearings or active magnetic bearings. Gas bearings allow for compact system integration with high load capacity and stiffness; but their application at high rotational speeds is limited by their poor dynamic stability. Active magnetic bearings facilitate a precise control of the rotor dynamics; however, at the price of a substantially increased installation and system complexity. Aiming to combine the advantages of these two bearing technologies, a hybrid bearing approach is proposed using a self-acting gas bearing for providing the main load capacity in combination with a small-sized active magnetic damper to achieve stable operation at high operational speeds. In order not to impair the compactness of the resulting drive system, dedicated displacement sensors are avoided by employing an eddy-current-based self-sensing rotor displacement measurement method using high-frequency signal injection. A previously proposed eddy-current-based self-sensing method is refined and implemented; measurement results are presented for a prototype machine proving the feasibility of the proposed hybrid bearing approach.**

***Index Terms*—Active magnetic damper (AMD), gas bearing, high-speed permanent-magnet machines, self-sensing, signal injection, vibration control.**

I. Introduction

INCREASING number of ultrahigh-speed electrical drive systems are being used in industrial applications, such as turbo-compressors in heat pumps, fuel cells, generators for portable gas or air turbines, and cryogenic systems [1]–[3]. Electrical drives with rotational speeds ranging from 200 000 revolutions per minute (r/min) to 1 000 000 r/min at power ratings of a few tens of watts to a few kilowatts are being considered for these emerging applications [4]. Further applications of ultrahigh-speed electrical machines include optical devices and flywheels as well as micromachining spindles, medical, and dental drills [5]. An overview of ultrahigh-speed applications is given in [6].

Challenges involved with ultrahigh-speed electrical machine design are of electromagnetic, thermal, elastic, and rotordynamic nature [7]. Thus, machine designs that are optimized in a multiphysics approach to have low losses at high speeds as well as a robust rotor construction in order to cope with rotor dynamics and the high centrifugal stresses under rotation have been presented in [8]–[10].

Up to now, the wide industrial application of such ultrahigh-speed drive systems has been hindered mainly by the lack of low-cost and reliable bearings that can feature a long lifetime at high rotational speeds. Today, bearing technologies employed at elevated speeds are ball bearings, gas bearings, and magnetic bearings.

Commercially available ball bearings can be used in applications at the lower end of the mentioned speed range, especially where a total life time of some hundreds of hours is sufficient, such as in medical or dental tools. However, due to high wear at high rotational speeds, ball bearings do not meet the lifetime requirement for most of the mentioned miniature scale applications at the top end of the specified rotational speed range.

Top speeds reached with active magnetic bearings are reported as 150 kr/min in [12] and 505 kr/min in [13]. Due to the contactless operation, high rotational speeds impose no inherent lifetime limitation; however, active magnetic bearings usually increase the installation size and the overall complexity of the system considerably with the need of displacement sensors, actuators, power amplifiers, and their control as well as an emergency touch-down bearing system.

Gas bearings exist as externally pressurized or self-acting types. In an externally pressurized bearing, the rotor is carried by the fluid film generated by an external pressurized air supply fed through orifices into the bearing clearance. In a self-acting bearing, the fluid film is formed by viscous shear forces resulting from the relative motion of journal and bushing under rotation. An external pressurized air supply is not needed and therefore

Manuscript received May 24, 2016; revised August 23, 2016; accepted October 11, 2016. Date of publication November 24, 2016; date of current version March 8, 2017.

A. Looser and C. Zwyssig are with Celeroton Ltd., 8604 Volketswil, Switzerland (e-mail: andreas.looser@celeroton.com; christof.zwyssig@celeroton.com).

A. Tüysüz and J. W. Kolar are with the Power Electronic Systems Laboratory, Swiss Federal Institute of Technology (ETH), Zurich, 8092 Zurich, Switzerland (e-mail: tuysuz@lem.ee.ethz.ch; kolar@lem.ee.ethz.ch).

Color versions of one or more of the figures in this paper are available online at http://ieeexplore.ieee.org.

Digital Object Identifier 10.1109/TIE.2016.2632680

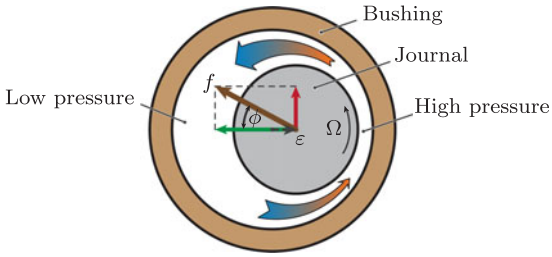

Fig. 1. Working principle of a gas lubricated plain journal bearing: When the journal is displaced, the air is dragged into the converging gap, which generates a pressure distribution leading to a force that restores the journal to its centered position [11].

the self-acting gas bearing allows for a very compact design. As Fig. 1 illustrates for the case of a plain journal bearing, the displacement of the rotating journal by ε leads to the fluid being dragged into the converging gap, which generates a high pressure. Contrarily, a lower pressure occurs on the diverging side. Hence, a net force acts on the journal, restoring it to its centered position. Compared to magnetic bearings, gas bearings can usually be designed much smaller for the same load capacity and stiffness, leading to more compact drive systems.

Rotational speeds above 1-million r/min have been reached with rotating machinery supported by externally pressurized or self-acting gas bearings. A wave-shaped self-acting gas bearing design achieving a rotational speed of 1203 kr/min is presented in [14]. Testing of a foil bearing operated at speeds up to 700 kr/min is reported in [15]. In these two bearing tests, helium and air turbines were used to drive the test rotors. When supporting the rotors of permanent-magnet machines, the achieved rotational speeds are lower, which can be related to the higher rotor weight that usually lowers instability onset speeds. For the mentioned wave-shaped gas bearing design applied to a permanent-magnet machine with a rated power of 200 W, a maximum speed of 410 kr/min is achieved in [16]. Foil bearings supporting the rotor of a permanent-magnet machine at a speed of 350 kr/min are reported in [17].

As visualized in Fig. 1, the restoring force of a gas bearing usually applies with an angle ϕ to the displacement vector ε, which is called the bearing's attitude angle. Therefore, a destabilizing azimuthal force component exists perpendicular to the journal displacement, since the restoring force f is not a purely radial force toward the bearing center. This force component, together with the relatively low damping from the fluid film itself, is the main cause of instability. A common remedy in gas bearing design for increasing the damping and achieving stability with heavier rotors at high speeds is to reduce the bearing clearance. This strategy, however, is limited for machines in the targeted speed and power range where the required bearing clearances scale to unfeasibly small dimensions and tight production tolerances. Another limitation affecting such bearing designs is high viscous friction losses and the resulting thermal distortion of shaft, bushing, and machine housing, which affects the bearing clearance and deteriorates bearing alignment.

It is possible to avoid the stringent manufacturing tolerances and high viscous friction losses together with their consequences on the bearing performance by introducing a controllable damper element [18]. This can be realized by using a hybrid bearing approach that combines the load capacity of gas bearings with the controllability of active magnetic bearings. The gas bearing is utilized as the main load carrying element, while a small-sized active magnetic bearing is used for stabilization—thus, it is called an active magnetic damper (AMD). Initial considerations regarding this concept have been discussed in [11], to provide a basis for vibration control of gas bearings supporting high-speed permanent-magnet electrical machines. In the same work, a signal-injection-based rotor displacement measurement method is also proposed for utilizing the AMD windings as eddy-current displacement sensors. Measurements taken at low speeds, where the gas bearing does not require an active stabilization (22 kr/min), are shown to verify the validity of the both displacement sensing and gas bearing concepts.

In this paper, the hybrid bearing concept is further improved toward stable operation at high-speeds. The design of the prototype machine is detailed in Section II. An improved circuit topology is presented in Section III for rotor displacement sensing, which decreases the cross-talk between the AMD currents and the injected current for displacement measurement. Section IV discusses the stabilization of the bearing-rotor system by feedback control. Finally, measurement results of the prototype machine in closed-loop operation at 210 kr/min are presented in Section V. The paper concludes in Section VI.

II. Machine Design

The design of the machine is according to prior work [19], where a high-efficiency permanent-magnet machine design is proposed for ultrahigh-speed applications. The key attributes of the machine are strongly related to minimizing the losses at high rotational speeds. Thus, it incorporates a slotless air gap winding to avoid slot-harmonic-induced rotor eddy-current losses. Windings are made of stranded (litz) wires in order to limit the proximity losses due to the permanent-magnet field. Amorphous iron laminations are employed for the stator back iron in order to limit the core losses.

To cope with the high centrifugal stresses, the brittle permanent magnet of the rotor is encased into a steel sleeve by interference fit.

The machine has a single pole pair; thus, the permanent magnet is diametrically magnetized, making it ideal for integrating a heteropolar active magnetic bearing winding, which is also realized as an air gap winding, directly into the machine [20]. This leads to a short rotor design that is beneficial for rotor dynamics and reduced windage losses. The same winding structure is used in this paper to realize the AMD. The damper windings are located at the cylindrical interior of the motor winding. They produce a fundamental current distribution with a pole-pair number of two, such that the interaction with the one pole-pair field of the permanent-magnet field generates Lorentz forces on the damper winding, and a reaction force is obtained on the rotor accordingly. On the other hand, the motor winding has only one pole-pair, hence it produces a force couple, thereby generating the drive torque on the rotor. Fig. 2 shows the cross-sectional view of the machine and depicts the force and torque generation by the AMD and motor windings, respectively.

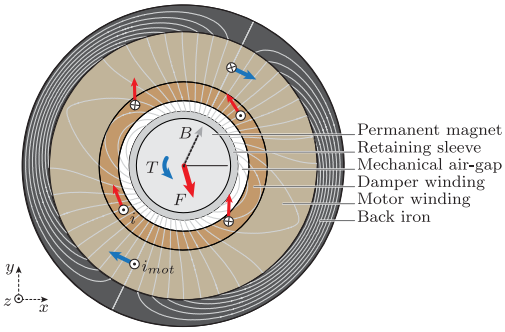

Fig. 2. Force and torque generation with a two-pole-pair AMD winding and a one-pole-pair machine winding using a diametrically magnetized rotor [11].

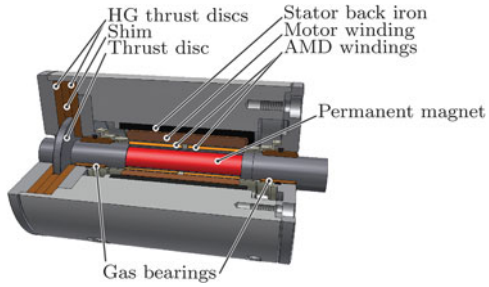

Fig. 3. Section view of the prototype machine with the hybrid gas-magnetic bearing concept.

Two possible air gap winding types are considered for the machine prototype, namely the skewed-type and the straight-type winding. The skewed-type three-phase winding with one pole pair generates besides a driving torque T_z in the principal axis also a transverse torque T_{xy} in the perpendicular plane, which results from the skewed arrangement of the conductors [21]. While T_z is the intended machine torque, the transverse torque T_{xy} is parasitic and needs to be compensated by the bearing system. For the present machine, a ratio of $T_{xy}/T_z \approx 0.5$ can be expected when using a skewed winding. In order to minimize any possible excitation forces that might interfere with the bearing system, the straight-type winding, which does not produce a transverse torque, is chosen for the prototype machine.

The damper windings serve two purposes, they generate the damping forces and at the same time they are used to sense the radial displacement of the rotor. The damper windings are arranged as close to the rotor surface as possible, which is beneficial for two reasons. First, damper forces can be generated with lower ohmic losses than at a larger diameter. Torque generation, on the other hand, is nearly not impaired due to the larger diameter of the motor winding as the lever arm is also elongated. Second, displacement measurement sensitivity of the damper winding is the highest at the smallest clearance to the rotor.

A CAD drawing of the prototype machine with gas bearings and magnetic dampers is shown in Fig. 3. The gas bearings are arranged close to the active region of the machine in order to keep the rotor short. The bearing bushings are supported on o-rings in order to enable self-alignment of the bushings. The damper windings are integrated into the active region of the machine. The motor winding is located around the damper windings. Axial rotor support is given by a thrust bearing implemented as a disc on the rotor which is kept in place between two herringbone-grooved (HG) thrust discs. The machine design parameters are given in Table I.

TABLE I
PROTOTYPE MACHINE DATA

Permanent-magnet radius	2.75 mm
Rotor radius	3 mm
Damper winding inner radius	3.25 mm
Motor winding inner radius	3.7 mm
Stator back iron inner radius	6 mm
Stator back iron outer radius	7.5 mm
Permanent magnet length	22 mm
Damper active length	10 mm
Journal bearing nominal clearance	8 μm
Rotor weight	12.3 g
Machine phase resistance	0.2 Ω
Machine phase inductance	4 μH
Machine flux linkage	0.2 mVs
Damper force constant	0.3 N/A
Damper inductance phase A (10 kHz)	4×2.6 μH
Damper inductance phase B (10 kHz)	11.6 μH
Damper resistance phase A	4×3.5 Ω
Damper resistance phase B	9.0 Ω

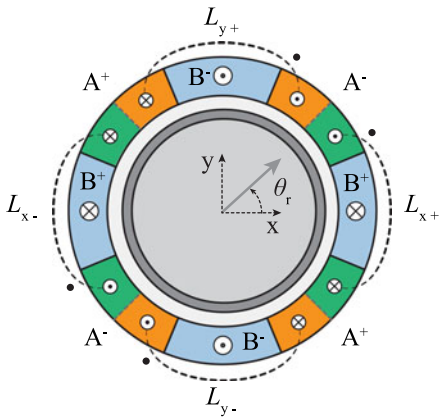

Fig. 4. Winding scheme of the two-phase (phase A, phase B) magnetic damper winding with oppositely arranged coil pairs for eddy-current-based high-frequency signal injection displacement sensing. Phase A is split into four coils arranged in pairs opposite to each other with reference to the rotor. The coil pair L_{x+}, L_{x-} (in green color) measures the displacement in *x*-direction and coil pair L_{y+}, L_{y-} (in orange color) in *y*-direction. Phase B (in blue color) is not used for displacement sensing.

III. SIGNAL-INJECTION-BASED DISPLACEMENT MEASUREMENT

As mentioned above, besides producing damping forces, the AMD windings also serve as eddy-current sensor heads. A suitable winding configuration for this purpose is shown in [11]. As seen in Fig. 4, the winding contains two phases, where one phase (phase A) is split into four coils L_{x+}, L_{x-}, L_{y+}, and L_{y-}. The coils are arranged in pairs opposite to each other with reference to the rotor, the coil pair L_{x+}, L_{x-} measures the

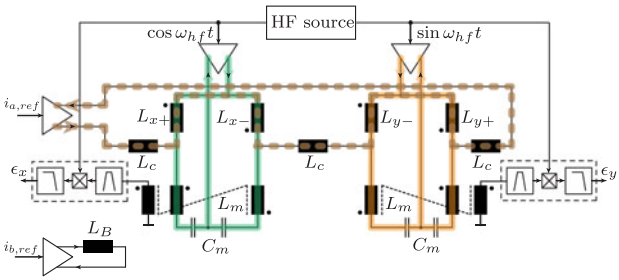

Fig. 5. Eddy-current-based displacement sensing topology with auxiliary signal injection and extraction circuits. The damper current is flowing through the series-connected coils L_{x+}, L_{x-}, L_{y+}, and L_{y-} of phase A (dashed brown line) but not through the measurement inductor L_m. The high-frequency signals are superimposed by means of capacitive coupling through C_m (green and orange lines). The inductors L_c are required for signal separation.

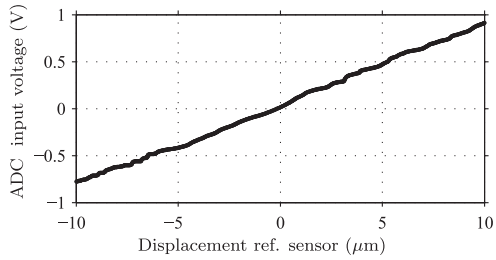

Fig. 6. Calibration of the eddy-current displacement signal captured at the input of the DSP-internal ADC with a commercial laser triangulation sensor displacement measurement.

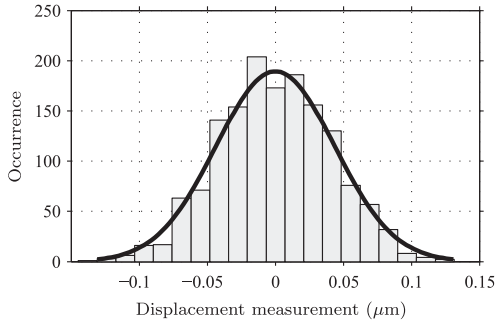

Fig. 7. Histogram with fitted normal distribution for the rotor displacement measurement with a stationary rotor based on a total of 1500 samples recorded by means of the DSP-internal 12-bit ADC at a sampling rate of 83 kHz.

displacement in x-direction and coil pair L_{y+}, L_{y-} in y-direction. The impedance of a coil decreases when the rotor is displaced in its direction (i.e., approaches to the coil), while the impedance of its counterpart increases. When the coils of a coil pair are connected in parallel, an injected high-frequency current will split into the two branches according to their impedance, depending on the instantaneous rotor displacement. The amplitude of the difference of the two high-frequency currents is therefore directly related to the rotor displacement.

Naturally, besides the high-frequency current for displacement measurement, the damper currents from the damper power amplifiers also need to be injected into the windings. A circuit topology for the superposition of the AMD current and the high-frequency current has been proposed in [11], where differentially coupled inductors are used to detect the displacement-dependent impedance change of the two oppositely arranged AMD coils and to produce a high-frequency signal with an amplitude proportional the radial displacement of the rotor. A major disadvantage of this method is that the AMD coils and the differentially coupled measurement inductors are connected in series regarding the damper current. Hence, the high-frequency signal may be amplitude modulated also through the current dependency of the measurement inductor's inductance. This cross-talk between the damper current and the displacement measurement signal hinders feedback control with the AMD.

In this paper, the aforementioned drawback is avoided by the modified circuit topology depicted in Fig. 5. For signal separation of the damper and the high-frequency measurement current, the large gap between the frequency bands of the two signals are exploited since the damper current frequencies range from dc to some tens of kilohertz, whereas the measurement current frequency is in the range of a few megahertz. The damper current is not flowing through the measurement inductor L_m anymore but through the coils L_c, which are needed to prevent leakage of the high-frequency measurement current to the AMD power amplifiers. A low-impedance path is provided for the high-frequency current by the differentially coupled measurement inductors L_m and the capacitors C_m. These represent a high-impedance at low frequencies and thus AMD current through L_m is avoided.

The voltage of the third coil of L_m is proportional to the difference of the currents in the first two coils, hence, its amplitude is proportional to the rotor displacement. In order to obtain the displacement signals, the known steps of amplitude demodulation, i.e., bandpass filtering, frequency mixing, and low-pass filtering are applied.

Fig. 6 shows the results of a calibration measurement of the prototype electronics and the machine, captured at the input of the internal analog-to-digital converter (ADC) of the digital signal processor (DSP) with a Keyence LK-H022 triangulation sensor as a reference. The measurement shows a sensitivity of 84 mV/μm.

For feedback control, only the derivative of the displacement is used; therefore, the absolute resolution of the eddy-current displacement measurement is not needed and a slow drift of the signal is of minor importance. The resolution of the measurement is therefore only related to the measurement noise. To quantify the measurement noise, the rotor is kept fixed at an arbitrary position while the signal is recorded by means of the internal 12-bit ADC of the DSP at a sampling rate of 83 kHz. A measurement standard deviation of $\sigma = 44$ nm is achieved; the corresponding histogram of 1500 samples is depicted in Fig. 7.

These results are nearly not affected by the presence of a sinusoidal AMD current in the damper windings. The measurement standard deviation increases to only $\sigma = 53$ nm at frequencies between 10 Hz and 10 kHz when the maximum current with an amplitude of 350 mA (thermal limit current) is flowing through the damper windings. For these tests, an unmagnetized rotor is used to avoid actual displacement due to Lorentz forces.

IV. Control

With gas bearings, the bearing properties can spread widely due to the high sensitivity to dimensional deviations under feasible manufacturing tolerances or varying operating conditions such as ambient pressure or temperature of the fluid. Thus, for being insusceptible to modeling errors of the controlled system, a D-type feedback controller which provides forces proportional to translational velocity of the rotor and therewith dissipates the energy of the whirling motion seems to be a promising approach to regain or improve stability of rotors supported by gas bearings at high-rotational speeds.

The influence of bearing stiffness, attitude angle, and damping on the stability of a rotor-bearing system can be illustrated with a simple model consisting of a single bearing supporting a concentrated mass that represents the rotor. The system has two degrees of freedom, namely the translational motion in x- and y-directions, represented by the real and imaginary parts of the complex displacement ϵ. The bearing-mass system can be described by the differential equation

$$m\ddot{\epsilon} = c_j \cdot \epsilon + f_\delta \tag{1}$$

where f_δ denotes an arbitrary disturbance force and c_j is the dynamic bearing stiffness of the bearing. In Laplace domain, the transfer function from the disturbance force to the displacement is then written as

$$\frac{\epsilon}{f_\delta} = \frac{1}{ms^2 - c_j(s)}. \tag{2}$$

The bearing stiffness may be assumed as

$$c_j = -c_s e^{j\phi} - d \cdot s \tag{3}$$

where $c_s e^{j\phi}$ denotes a static bearing stiffness with attitude angle ϕ, i.e., $c_s e^{j\phi}$ contains a restoring component $c_s \cos(\phi)$ and a cross-coupling component $c_s \sin(\phi)$. The factor d is the damping factor which yields a force proportional to the velocity. The poles are given by the roots of the system's characteristic polynomial which are

$$p = \frac{-d \pm \sqrt{d^2 - 4mc_s e^{j\phi}}}{2m}. \tag{4}$$

Stability is given if $\Re\{p\} < 0$ which implies that the inequality

$$\Re\left\{\sqrt{1 - \frac{4mc_s e^{j\phi}}{d^2}}\right\} < 1 \tag{5}$$

must hold.

The above inequality can be solved for the maximum allowable attitude angle ϕ, given a supported mass m, a static stiffness c_s, and a damping ratio d. The obtained result is plotted in Fig. 8. Attitude angles above the indicated boundary result in unstable systems while smaller attitude angles yield stability. On the limit line, the system is boundary stable. For small values of $\frac{mc_s}{d^2}$, the attitude angle ϕ which still yields stability approaches 90°, while for large values of $\frac{mc_s}{d^2}$, ϕ needs to be gradually decreased.

It can be seen that for a heavier supported mass m, stability is harder to achieve and a smaller attitude angle or higher damping may be required. It can be concluded that a bearing with a positive restoring stiffness and any amount of cross-coupling stiffness can always be stabilized by providing sufficient damping, either from within the fluid film or from an external source such as by AMDs with feedback control. The example shows that increasing the damping in the system, e.g., with D-type control, is a very general means to improve the stability of gas bearing supported rotors; and it is widely independent of gas bearing properties which might not be known exactly.

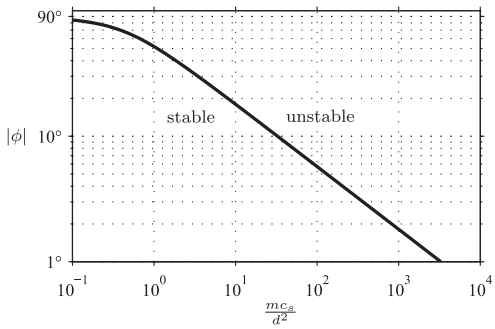

Fig. 8. Stability limit for the bearing attitude angle ϕ depending on the supported mass m, static bearing stiffness c_s, and the damping factor d.

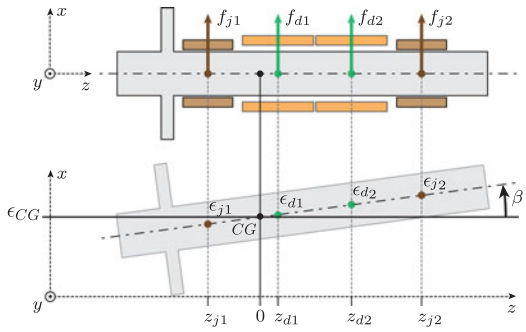

Fig. 9. Rotor with gas bearings and AMD actuators: Definition of forces f and displacements ϵ. The gas bearings are indicated in brown and the AMD actuator windings in orange color.

In order to estimate the required damping ratio for stabilizing the rotor of the prototype system, a rigid body rotor model is used. The state of the rotor is defined by the radial displacement of its center of gravity ϵ_{CG} and the inclination angle β, as shown in Fig. 9. The gas bearing forces denoted as f_{j1} and f_{j2} act at the locations z_{j1} and z_{j2}; and the damper forces denoted as f_{d1} and f_{d2} act at the locations z_{d1} and z_{d2}.

Governing equations of motion for a rigid rotor can be found, e.g., in [22]. Assuming rotational symmetry, these equations can be written in a complex form. With a complex definition of the displacement, which is defined by the displacements in x- and y-direction as $\epsilon = \epsilon_x + j\epsilon_y$, and the complex inclination angle $\beta = \beta_x + j\beta_y$, they can be formulated as

$$m\ddot{\epsilon}_{cg} = f_{j1} + f_{j2} + f_{d1} + f_{d2} \tag{6}$$

$$I_{x0}\ddot{\beta} - j\Omega I_{z0}\dot{\beta} = z_{j1} \cdot f_{j1} + z_{j2} \cdot f_{j2} + z_{d1} \cdot f_{d1} + z_{d2} \cdot f_{d2} \tag{7}$$

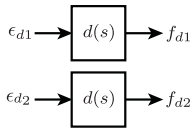

Fig. 10. Block diagram of the D-type feedback controller.

where m is the rotor mass, I_{x0} is the inertia of the rotor about the x-axis (same as about the y-axis), I_{z0} is the inertia about the $z-$ axis, and Ω denotes the angular velocity of the rotor. The term $j\Omega I_{z0}\dot{\beta}$ describes a cross-coupling torque between the x- and y-axis, respectively between the real and imaginary axis, which originates from gyroscopic forces.

The D-type controller takes the displacements at the damper location as inputs and generates reference forces as outputs, according Fig. 10.

The transfer function of the D-type controller is

$$d(s) = K_d \cdot \frac{s}{\frac{s}{\omega_c} + 1} \tag{8}$$

where K_d is the damping ratio and ω_c is the cutoff frequency of the controller to limit damping at high frequencies and avoid excessive noise.

Without active magnetic damping, the gas-bearing rotor system with a nominal design clearance of $c = 8$ μm is expected to become unstable at around 240 kr/m. Taking into account production deviations of the bearing clearance $c = 8 \pm 2$ μm, the system is expected to be unstable already at around 120 kr/m as is apparent from the root locus plots of the systems in Fig. 11(a) and (b), respectively. With a D-type controller with parameters $K_d = 20$ N $\cdot$ s/m and $\omega_c = 6.3 \cdot 10^3$ rad/s, the system can be stabilized. The frequency response of the D-type controller together with the expected nominal design bearing response is shown in the Bode diagram of Fig. 12.

The root locus plot of the stabilized system is shown in Fig. 11(c). Comparing to the root locus plot of the nonstabilized systems, all the unstable poles are shifted into the left-half plane (LHP). For low speeds, the damper is relatively strong compared to the restoring force of the gas bearing, hence poles exist close to the origin, i.e., with the low stiffness of the gas bearing, a displaced rotor will converge slowly only to the bearing's center as motion is heavily damped by the magnetic damper. For higher speeds, the gas bearing gains strength and the poles move further into the LHP. Three of the originally four relevant modes have moved moderately into the LHP, the fourth mode is now far in the LHP and is therefore not depicted.

V. Hardware Implementation and Experimental Results

The damper electronics containing the displacement measurement signal processing and angular rotor position detection circuits (as detailed in [11]) as well as the damper power amplifiers and a DSP for control are implemented on a 80 $\times$ 100 mm^2 four-layer printed circuit board (PCB). The damper amplifiers are realized by linear power amplifiers OPA548 operated from a

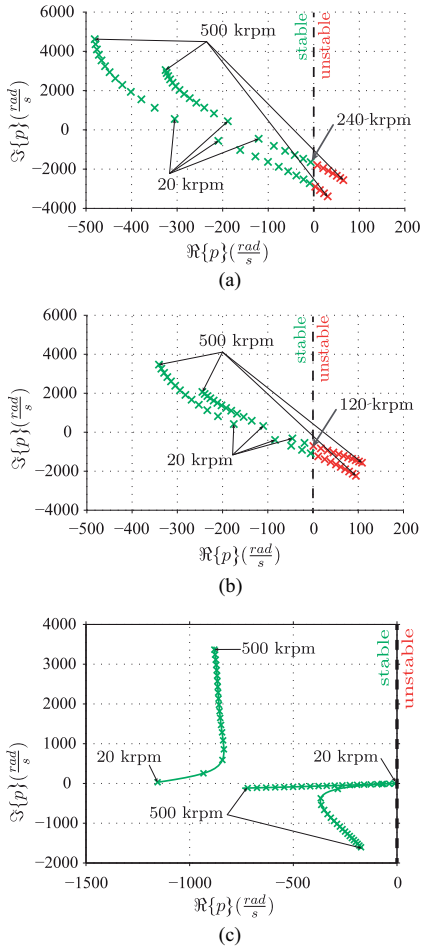

Fig. 11. Speed-dependent root locus plot of the relevant closed-loop poles of the rotor gas bearing system with the (a) nominal gas bearing design without AMD, (b) a gas bearing tolerated production deviations without AMD and (c) with AMD.

± 8 V dual supply, while the displacement signal processing and the angular position detection circuits are running from a single 5 V supply. Signal injection occurs at distinct frequencies (at 10 and 12 MHz) for the two damper windings to avoid interference.

A Texas Instruments TMS320F2808 DSP with a 32-bit fixed-point architecture is used to implement the control. The control loop containing signal acquisition with the DSP's internal 12-bit ADC, the actual control with the displacement's derivative, the notch filtering, and the transformation of the qd-reference currents into the phase reference currents is executed at a rate of 83 kHz. The low-pass filter of the displacement signal demodulation stage, which defines the measurement bandwidth, is implemented as a second-order low-pass filter with a cutoff frequency of 35 kHz. A digital-to-analog converter interface is connected to the DSP via a serial peripheral interface in order to monitor system variables during measurements. A photograph of the electronics and the prototype machine with installed dampers is shown in Fig. 13.

Among the fixed geometry gas bearings which are favored for reasons of production, the HG journal bearing and the Rayleigh-step journal bearing were considered for the prototype

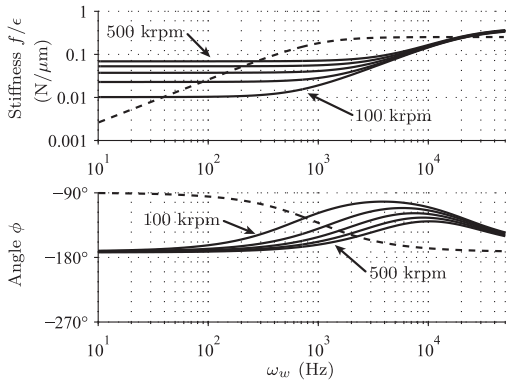

Fig. 12. D-type controller frequency response (dashed line) with $K_d = 20\ \mathrm{N \cdot s/m}$, $\omega_c = 6.3 \cdot 10^3$ rad/s, and nominal design gas bearing frequency response at 100, 200, 300, 400, and 500 kr/min for comparison (solid lines).

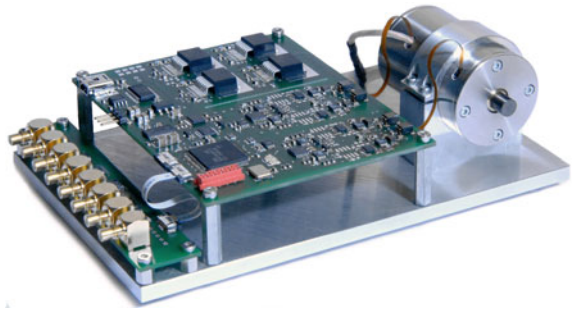

Fig. 13. Prototype permanent-magnet machine with installed gas bearings, AMDs, and electronics. The PCB size is 80 × 100 mm^2.

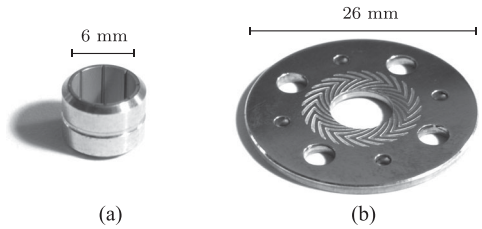

Fig. 14. (a) Prototypes of the Rayleigh-step journal bearing and (b) HG thrust disc.

machine. With HG journal bearings, the herringbone pattern needs to be structured on the rotor to obtain the superior stability. Unfortunately, structuring the rotor with the herringbone micropattern represents a further step in the already complex rotor fabrication.

Fabrication of a Rayleigh-step structure can be achieved relatively easily by wire electrical discharge machining (EDM) the bearing bushing as the structures occur in axial direction only. Only a few preceding fabrication steps are needed for the bushing before wire EDM, which is the last and the only high precision fabrication step. Thus, a Rayleigh-step bearing is chosen for the prototype machine, as shown in Fig. 14(a). The thrust bearing is implemented as an unstructured disc on the rotor and two HG discs on the stator. Fig. 14(b) shows the HG discs manufactured by photo lithography.

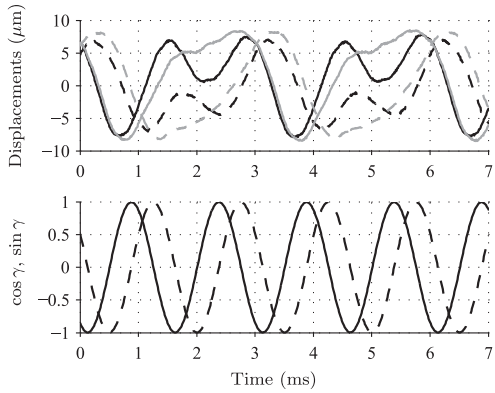

Fig. 15. Displacement signals measured with the DSP at 40 kr/min with inactive damper (top), $\epsilon_{d1,x}$ (solid black), $\epsilon_{d1,y}$ (dashed black), $\epsilon_{d2,x}$ (solid gray), $\epsilon_{d2,y}$ (dashed gray). The gas bearings operate in a whirl condition with a frequency of half of the rotational speed. As a reference, the rotor's angular position in terms of $\cos\gamma$ (solid line) and $\sin\gamma$ (dashed line) is also shown (bottom).

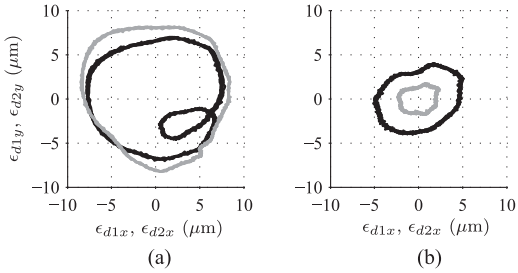

Fig. 16. (a) Orbit plots of displacements (ϵ_{d1} black, ϵ_{d2} gray) measured by the DSP (a) with inactive damper at 40 kr/min and (b) with active magnetic damping at the same rotational speed.

Under operation, the rotor of the prototype machine lifts off at around 10 kr/min. Without active magnetic damping, instability onset occurs at around 30 to 40 kr/min, clearly visible in the displacement measurement in Fig. 15 as whirling with a frequency of half the rotational speed and corresponding orbit in Fig. 16(a). Also a fundamental-frequency component is visible in the displacement measurement, which originates from rotor unbalance. The onset of instability occurs at a lower speed than expected, which can be attributed to production deviations and unbalance in combination with the nonlinear displacement-to-force characteristics of the bearing, which were not accounted for in the bearing selection and design phase. Nevertheless, with the AMD system, the gas-bearing rotor system can be effectively stabilized. With active magnetic damping, the orbit plots in Fig. 16(b) are obtained, which show much smaller diameter, which is now only given by the rotor unbalance, as the rotor rotates about its center line of gravity.

A maximum speed of 210 kr/m is achieved with the current gas bearing design. Fig. 17 shows the measured displacements together with the damper currents and the angular rotor position signals. The amplitude of the displacement signals mainly show a synchronous-frequency component, which is caused by the rotor's residual imbalance. Also, increased noise is visible on the displacement measurement which is caused primarily by the damper currents $i_{a,1}$ and $i_{a,2}$.

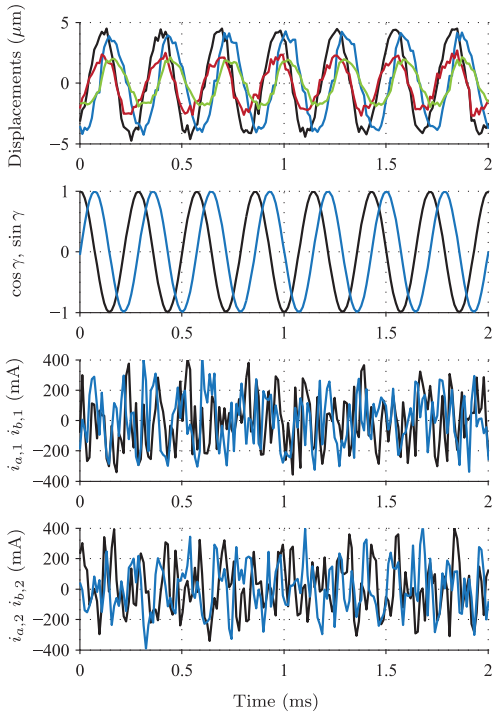

Fig. 17. Measurement of the rotor displacements $\epsilon_{d1,x}$ (black), $\epsilon_{d1,y}$ (blue), $\epsilon_{d2,x}$ (red), and $\epsilon_{d2,y}$ (green) at 210 kr/min along with the angular rotor position signals $\cos\gamma$ (black) and $\sin\gamma$ (blue) and the damper winding currents $i_{a,1}$ (black), $i_{b,1}$ (blue) and $i_{a,3}$ (black), $i_{b,3}$ (blue).

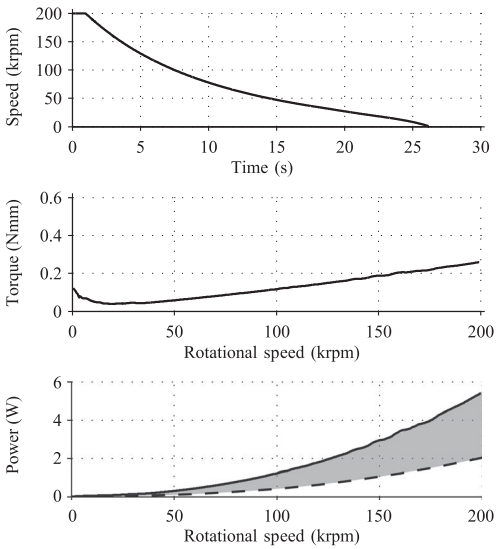

Fig. 18. Deceleration test of the prototype machine from 200 kr/min for obtaining the no-load losses. Speed recorded over time (top), speed-dependent braking (loss) torque (middle), and resulting no-load losses (solid line, bottom) with the calculated machine no-load losses (dashed line, bottom). The shaded gray area represents the gas bearing losses.

Fig. 18 shows the no-load losses of the prototype machine, measured by a deceleration test [5]. The friction torque observed at low speeds results from the dry friction of the gas bearing before lift-off at around 20 kr/min. The friction torque is minimum around lift-off and increases again with higher speeds.

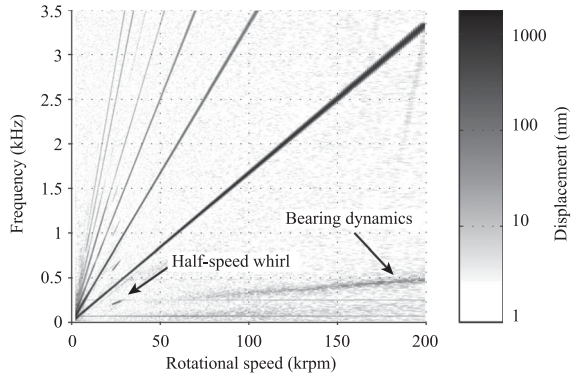

Fig. 19. Spectrogram of the displacement $\epsilon_{d1,x}$ recorded during deceleration.

Fig. 19 shows a spectrogram of the displacement $\epsilon_{d1,x}$ recorded during the deceleration test. The dominant displacement, which is visible as the straight black line, is the fundamental-frequency displacement resulting from rotor imbalance. Harmonics of the fundamental frequency are also present, which are attributed to the rotor surface out-of-roundness. The bearing dynamics are visible at frequencies below 500 Hz, with a slight increase of displacement visible in the frequency range toward higher speeds. Therefore, a higher amount of damping would be required in order to suppress these vibrations, when proceeding toward higher rotational speeds.

Damping required for stabilizing the gas bearings is approximately three times higher than what the calculations had predicted. The parameters of the transfer function $d(s)$ is set to $K_d = 60$ N s/m with $\omega_c = 12.6 \cdot 10^3$ rad/s to obtain stable operation.

A limiting factor that prevents increasing the speed further is related to the high controller gain required for stabilization. The very small but existing cross-talk between the damper current and the displacement measurement imposes a limit on the maximum achievable controller gain. With higher gains, the existence this of cross-talk would render the electrical system unstable. In order to reach even higher rotational speeds with the present magnetic damper design, a gas bearing with better stability requiring less magnetic damping would be needed.

VI. Conclusion

The use of ultrahigh-speed electrical drive systems in industrial applications has been restrained by the absence of a reliable bearing technology with long lifetime at rotational speeds ranging from 200 000 r/min up to 1 000 000 r/min. Possible bearing candidates for high rotational speeds are gas bearings and magnetic bearings, which avoid friction and wear due to their contactless operation. However, magnetic bearings usually impose a major installation size and increased system complexity, while gas bearings suffer from poor stability and stringent production precision and high friction losses.

With the proposed hybrid bearing approach that employs a gas bearing as the main load carrying element and a small-sized AMD for stabilization, production tolerances are relaxed and

excessive losses are avoided. Compactness of the drive system is maintained by integrating the AMD into the active region of the machine and by applying an eddy-current-based self-sensing method instead of using dedicated sensors for rotor displacement measurement. An improved electrical circuit topology was proposed for the superposition of the high-frequency current and the AMD current as well as implementation of the differential impedance measurements for obtaining the rotor displacement. A prototype machine employing the hybrid bearing system was presented and stabilization of the unstable gas bearing was successfully demonstrated up to 210 kr/min by means of active magnetic damping.

Future work will focus on the tradeoff between fabrication effort and the performance of gas bearings, considering the new possibility of active magnetic stabilization. While stable operation of a hybrid gas-magnetic bearing has been shown in a prototype demonstrator which is suited for industrial applications such as turbo-compressors with long steady-state operation times, the future work will also consider the transient performance of the proposed system.

References

[1] H. Mitterhofer, W. Gruber, and W. Amrhein, "On the high speed capacity of bearingless drives," *IEEE Trans. Ind. Electron.*, vol. 61, no. 6, pp. 3119–3126, Jun. 2014.

[2] D. Gerada, A. Mebarki, N. Brown, C. Gerada, A. Cavagnino, and A. Boglietti, "High-speed electrical machines: Technologies, trends, and developments," *IEEE Trans. Ind. Electron.*, vol. 61, no. 6, pp. 2946–2959, Jun. 2014.

[3] D. Krähenbühl, C. Zwyssig, and J. W. Kolar, "Half-controlled boost rectifier for low-power high-speed permanent-magnet generators," *IEEE Trans. Ind. Electron.*, vol. 58, no. 11, pp. 5066–5075, Nov. 2011.

[4] C. Zwyssig, S. D. Round, and J. W. Kolar, "An ultrahigh-speed, low power electrical drive system," *IEEE Trans. Ind. Electron.*, vol. 55, no. 2, pp. 577–585, Feb. 2008.

[5] A. Tüysüz, C. Zwyssig, and J. W. Kolar, "A novel motor topology for high-speed micro-machining applications," *IEEE Trans. Ind. Electron.*, vol. 61, no. 6, pp. 2960–2968, Jun. 2014.

[6] C. Zwyssig, J. W. Kolar, and S. D. Round, "Megaspeed drive systems: Pushing beyond 1 million r/min," *IEEE/ASME Trans. Mechatronics*, vol. 14, no. 5, pp. 564–574, Oct. 2009.

[7] A. Tenconi, S. Vaschetto, and A. Vigliani, "Electrical machines for high-speed applications: Design considerations and tradeoffs," *IEEE Trans. Ind. Electron.*, vol. 61, no. 6, pp. 3022–3029, Jun. 2014.

[8] C. Zwyssig, "An ultra-high-speed electrical drive system," Ph.D. dissertation, Dept. Inf. Technol. Elect. Eng., ETH Zurich, Zurich, Switzerland, 2008.

[9] A. Borisavljevic, "Limits, modeling and design of high-speed permanent magnet machines," Ph.D. dissertation, Faculty Elect. Eng., Math. Comput. Sci., Delft University of Technology, Delft, The Netherlands, 2011.

[10] P.-D. Pfister and Y. Perriard, "Very-high-speed slotless permanent-magnet motors: Analytical modeling, optimization, design, and torque measurement methods," *IEEE Trans. Ind. Electron.*, vol. 57, no. 1, pp. 296–303, Jan. 2010.

[11] A. Looser and J. W. Kolar, "An active magnetic damper concept for stabilization of gas bearings in high-speed permanent-magnet machines," *IEEE Trans. Ind. Electron.*, vol. 61, no. 6, pp. 3089–3098, Jun. 2014.

[12] M. Kimman, "Design of a micro milling setup with an active magnetic bearing spindle," Ph.D. dissertation, Faculty Mech., Maritime Mater. Eng., Delft University of Technology, Delft, The Netherlands, 2010.

[13] T. Baumgartner, R. Burkart, and J. W. Kolar, "Analysis and design of a 300-W 500 000-r/min slotless self-bearing permanent-magnet motor," *IEEE Trans. Ind. Electron.*, vol. 61, no. 8, pp. 4326–4336, Aug. 2014.

[14] T. Waumans, J. Peirs, F. Al-Bender, and D. Reynaerts, "Aerodynamic journal bearing with a flexible, damped support operating at 7.2 million DN," *J. Micromech. Microeng*, vol. 21, no. 10, 2011, Art. no. 104014.

[15] M. Salehi, H. Heshmat, J. F. Walton, and M. Tomaszewski, "Operation of a mesoscopic gas turbine simulator at speeds in excess of 700,000 rpm on foil bearings," *ASME J. Eng. Gas Turbines Power*, vol. 129, no. 1, pp. 170–176, 2007.

[16] J. Peirs, C. Zwyssig, T. Waumans, F. Al-Bender, and D. Reynaerts, "600000 rpm electrical motor/generator supported by air bearings," in *Proc. 12th Int. Workshop Micro- Nanotechnol. Power Gener. Energy Convers. Appl.*, Dec. 2012, pp. 165–168.

[17] D. Kim, M. S. Hossain, S.-J. Son, C.-J. Choi, and D. Krähenbühl, "Five millimeter air foil bearing operating at 350,000 rpm in a micro electric motor drive," in *Proc. AMSE/STLE Int. Joint Tribol. Conf.*, Oct. 2011, pp. 163–166.

[18] A. Looser, "Gas bearing with active magnetic damping for ultra-high-speed electrical drive systems," Ph.D. dissertation, Dept. Inf. Technol. Elect. Eng., ETH Zurich, Zurich, Switzerland, 2013.

[19] J. Luomi, C. Zwyssig, A. Looser, and J. W. Kolar, "Efficiency optimization of a 100-W 500 000-r/min permanent-magnet machine including air-friction losses," *IEEE Trans. Ind. Appl.*, vol. 45, no. 4, pp. 1368–1377, Jul./Aug. 2009.

[20] T. Baumgartner, R. Burkart, and J. W. Kolar, "Analysis and design of an ultra-high-speed slotless self-bearing permanent-magnet motor," in *Proc. 38th Annu. Conf. IEEE Ind. Electron. Soc.*, Oct. 2012, pp. 4477–4483.

[21] A. Looser, T. Baumgartner, J. W. Kolar, and C. Zwyssig, "Analysis and measurement of three-dimensional torque and forces for slotless permanent-magnet motors," *IEEE Trans. Ind. Appl.*, vol. 48, no. 4, pp. 1258–1266, Jul./Aug. 2012.

[22] G. Schweitzer and E. Maslen, *Magnetic Bearings: Theory, Design, and Application to Rotating Machinery*, New York, NY, USA: Springer, 2009.

Andreas Looser (M'14) received the M.Sc. degree in electrical engineering from the Swiss Federal Institute of Technology (ETH) Zurich, Zurich, Switzerland, in 2007, and the Ph.D. degree for his research on ultrahigh-speed electrical drive systems and bearing technology from the Power Electronic Systems Laboratory, ETH Zurich, in 2013.

Since 2013, has been with Celeroton AG, Volketswil, Switzerland, a company specializing in high-speed electrical drive systems, where he is working on electrical machine and bearing technology. His research interests include mechatronics, power electronics, control, and microelectronics.

Arda Tüysüz (M'13) received the B.Sc. degree in electrical engineering from Istanbul Technical University, Istanbul, Turkey, in 2006, the M.Sc. degree in electrical power engineering from RWTH Aachen University, Aachen, Germany, in 2009, and the Ph.D. degree in electrical drives from the Swiss Federal Institute of Technology (ETH) Zurich, Zurich, Switzerland, in 2015.

He is currently a Postdoctoral Researcher with the Power Electronic Systems Laboratory, ETH Zurich. His research interests include novel electrical machine topologies, self-sensing control of high-speed electrical machines, and wide-bandgap power devices for very efficient and compact electrical drive systems.

Christof Zwyssig (M'10) received the M.Sc. and Ph.D. degrees in electrical engineering from the Swiss Federal Institute of Technology (ETH) Zurich, Zurich, Switzerland, in 2004 and 2008, respectively. He studied power electronics, machines, and magnetic bearings and was engaged in research on high-speed electrical drive systems and their power electronics. He was with Chalmers University of Technology, Gothenburg, Sweden, where he was involved in the field of wind turbines. Since 2009, he has been with Celeroton AG, Volketswil, Switzerland, a company specializing in high-speed electrical drive systems, of which he is a cofounder.

Johann W. Kolar (F'10) received the M.Sc. degree in industrial electronics and control engineering and the Ph.D. degree in electrical engineering (*summa cum laude / promotio sub auspiciis praesidentis rei publicae*) from the Vienna University of Technology, Vienna, Austria, in 1997 and 1999, respectively.

Since 1984, he has been working as an Independent Researcher and an International Consultant in close collaboration with the Vienna University of Technology, in the fields of power electronics, industrial electronics, and high-performance drives. He was appointed as an Associate Professor and the Head of the Power Electronic Systems Laboratory, Swiss Federal Institute of Technology (ETH) Zurich, Zurich, Switzerland, on February 1, 2001, and was promoted to the rank of Full Professor in 2004. He has proposed numerous novel PWM converter topologies (e.g., the VIENNA Rectifier, Sparse Matrix Converter, and SWISS Rectifier), and modulation and control concepts. He has published more than 750 scientific papers in international journals and conference proceedings, three book chapters, and has filed more than 140 patents. He has presented more than 20 educational seminars at leading international conferences and served as an IEEE PELS Distinguished Lecturer from 2012 to 2016. He has supervised more than 60 Ph.D. students and has initiated and/or is the founder of four ETH spin-off companies. The focus of his current research is on ultracompact and ultraefficient SiC and GaN converter systems, wireless power transfer, solid-state transformers, power supplies on chip, as well as ultrahigh-speed and ultralightweight drives, bearingless motors, and energy harvesting.

Dr. Kolar has received 25 IEEE TRANSACTIONS and Conference Prize Paper Awards, the 2014 IEEE Power Electronics Society R. David Middlebrook Achievement Award, the 2014 SEMIKRON Innovation Award, the 2016 IEEE William E. Newell Power Electronics Award, and the ETH Zurich Golden Owl Award for excellence in teaching. He is a member of the Steering Committees of several leading international conferences in the field and served from 1997 to 2000 as an Associate Editor of the IEEE TRANSACTIONS ON INDUSTRIAL ELECTRONICS and from 2001 to 2013 as an Associate Editor of the IEEE TRANSACTIONS ON POWER ELECTRONICS. Since 2002, he also has been an Associate Editor of the *Journal of Power Electronics* of the Korean Institute of Power Electronics and a member of the Editorial Advisory Board of the *IEEJ Transactions on Electrical and Electronic Engineering*.